photonics

MDPI

Article

Symmetry-Breaking-Induced Quasi-Bound States in the Continuum in All-Dielectric Terahertz Metasurface for High-Sensitivity Refractive Index Sensing and Theoretical Virus Differentiation

Weinan Shi [1], Sibo Liao [1], Xipu Dong [2], Lu Zhang [1], Xiaoyu Zhu [1], Wenyan Nie [1], Zhong Ren [1,*], Xianghui Wang [3,*] and Jia Zhang [1,*]

[1] Jiangxi Provincial Key Laboratory of Advanced Electronic Materials and Devices, Jiangxi Science and Technology Normal University, Nanchang 330038, China; 1020240608@jxstnu.edu.cn (W.S.)
[2] Institute for Testing of Industrial Products of Jiangxi General Institute of Testing and Certification, Nanchang 330052, China
[3] Tianjin Key Laboratory of Micro-Scale Optical Information Science and Technology, Institute of Modern Optics, Nankai University, Tianjin 300350, China
* Correspondence: 1020101063@jxstnu.edu.cn (Z.R.); wangxianghui@nankai.edu.cn (X.W.); julyzhang2021@163.com (J.Z.)

Abstract

Bound states in the continuum (BIC) have recently attracted extensive research interest, owing to their exceptional capability for light confinement and high quality-factor (*Q*-factor) resonances. In this work, we design an all-dielectric terahertz metasurface based on the symmetry-breaking properties of silicon rectangular pillars. Numerical simulations demonstrate that breaking the in-plane inversion (C_2) symmetry transforms the BIC into a quasi-BIC (q-BIC), which features a high *Q*-factor and a narrow resonance linewidth. Through far-field multipole decomposition and near-field electromagnetic field distribution analysis, the excitation mechanism of the q-BIC mode is elucidated, revealing that the magnetic dipole (MD) contribution remains predominant over a certain range of asymmetry. Furthermore, the q-BIC resonance exhibits high sensitivity to the change in refractive index, achieving a theoretical sensitivity of 110 GHz/RIU even with an analyte thickness of only 15 μm. When MS2 and PRD1 bacteriophages are employed as model analytes with distinct effective refractive indices, the sensor produces a larger resonance frequency shift for MS2 than for PRD1, demonstrating its capability for theoretical dielectric discrimination based on refractive index differences. These findings provide a valuable reference for the development of all-dielectric terahertz metasurface platforms for label-free refractive index sensing and model virus differentiation.

Keywords: bound states in the continuum; all-dielectric metasurface; terahertz sensing; magnetic dipole; biosensing

Check for updates

Received: 7 September 2026
Revised: 21 September 2026
Accepted: 26 September 2026
Published: 29 September 2026

Copyright: © 2026 by the authors. Licensee MDPI, Basel, Switzerland. This article is an open access article distributed under the terms and conditions of the Creative Commons Attribution (CC BY) license.

1. Introduction

Biosensing plays a central role in disease diagnosis, food safety, and public health. A biosensor typically consists of two essential components: a biological recognition element (e.g., antibodies, aptamers, enzymes), and a physical transducer that converts the recognition event into a measurable signal. Among them, optical biosensors are particularly attractive because they enable label-free, real-time, and high-sensitivity detection [1].

Optical and photonic biosensors include plasmonic sensors [2], photonic crystal cavities [3], and metasurfaces-based sensors [4] et al. Their performance is commonly evaluated by sensitivity, figure of merit (FOM), limit of detection (LOD), and specificity. An important distinction must be made between surface and bulk sensing: surface-sensitive devices probe local refractive index changes near the transducer surface, whereas bulk sensors respond to the surrounding medium. For example, Panciera et al. present a refractive index sensor; the device achieves bulk sensitivity of 97 nm/RIU [5]. Functionalization, analyte volume, and compatibility with biological matrices also strongly affect practical performance [6]. In particular, refractive index (RI) sensors based on optical resonances can provide label-free detection, but they are not intrinsically specific. For example, Chen et al. designed an all-dielectric metasurface supporting multiple Fano resonances; the sensitivity can reach 402 nm/RIU, with a maximum figure of merit of 2400 RIU^{-1} [7]. Priya et al. present a biosensor based on 1D topological photonic crystals, which shows a sensitivity of 1500 nm RIU^{-1} with low limit of detection [8]. Without a selective recognition layer, any biological or non-biological analyte with a similar effective RI can produce a comparable response [9,10]. Therefore, an RI sensor should be regarded as a physical transducer rather than a complete biosensor unless a biorecognition element is incorporated.

Terahertz (THz) waves are non-ionizing and respond sensitively to the characteristics of biomolecules [11,12]. Moreover, many low-frequency vibrational modes of proteins, nucleic acids, and viruses located in the THz frequency range [13–15], rendering THz spectroscopy particularly valuable for biosensing and molecular recognition. However, traditional THz detection techniques suffer from drawbacks such as weak response, low signal-to-noise ratio, and insufficient sensitivity, which hinders high-sensitivity detection of minute biological samples [16]. Fortunately, the emergence of metasurfaces can effectively solve this problem.

Metasurfaces are artificial electromagnetic microstructures composed of periodically arranged subwavelength unit cells. By optimizing the geometry and arrangement of the units, one can tailor the propagation and localization of electromagnetic waves [17–19]. Careful design of the geometric parameters and material properties of metasurface elements enables the excitation of various resonance modes, including Fano resonance [20], electromagnetic induced transparency (EIT) [21], ring dipole resonance [22], anapole mode [23], and bound states in the continuum (BIC) [24] et al. For example, Singh et al. used THz metamaterials with Fano resonance to achieve ultra-sensitive refractive index sensing [25]; Zhang et al. developed a THz EIT metasurface for detecting intact H1N1 and H5N9 influenza virus particles, achieving a detection limit as low as 0.1 mg/mL (virus stock) [26]; Yang et al. designed a anapole mode metasurface to quantitatively characterize D-glutamic acid and D-lactose as well as their mixture [27]. These studies demonstrate that diverse resonance modes can significantly enhance the sensing performance for biomolecules. Among these modes, BIC has garnered particular attention in recent years due to its unique high quality-factor (Q-factor) characteristics.

BIC can confine energy in an open radiation environment. Theoretically, an ideal BIC exhibits an infinitely narrow linewidth resonance with an infinitely high Q-factor [28–31]. By introducing structural perturbations to break the symmetry of the system, BIC can be transformed into quasi-BIC (q-BIC) with finite radiation loss, which manifest as extremely narrow linewidths and high-Q resonances in the spectrum [32–34]. For example, Liu et al. proposed a q-BIC metasurface to detect L-Proline solutions in the concentration range of 0.1–1 mmo/L [35]. Due to the high-Q nature of q-BIC, it can excite significant local electromagnetic field enhancement and is highly sensitive to changes in the surrounding dielectric environment [36]. Consequently, BIC-based metasensors hold great promise for high-sensitivity biochemical sensing [37–40]. For instance, Huang et al. proposed

a graphene-based THz q-BIC biosensor, the detection limit reached 0.21 pg/mL in solutions [41]. Wang et al. also designed a THz sensor based on q-BIC metasurface [42], which allows for the detection of conjugated antibody-AuNPs for cardiac troponin I at concentrations as low as 0.5 pg/mL.

Currently, most research on THz BIC metasurfaces stays focused on metal structures. However, the use of metals to realize q-BIC inevitably introduces ohmic losses, increases non-radiative losses, and causes the actual *Q*-factor to deviate significantly from the theoretical value while also weakening local field enhancement. Moreover, Joule heating in metallic structures can impair device performance, which limits their application in high-sensitivity sensing [43]. In contrast, high-refractive-index dielectric materials can significantly reduce ohmic losses compared with metallic structures, facilitating the realization of high-*Q* resonances. Furthermore, metallic structures are typically confined to simple, regular geometries, whereas all-dielectric q-BIC architectures offer more tunable parameters and greater design flexibility [44,45], which further enhances sensing performance [46]. In the THz range, silicon-based nanostructures feature low loss, strong field confinement, and ease of integration, making them a robust platform for developing all-dielectric THz metasurfaces [47]. To date, silicon-based all-dielectric q-BIC metasurfaces have been successfully employed for high-sensitivity refractive index sensing and have demonstrated favorable detection performance, showing great potential for THz biosensing applications. Nevertheless, the influence of structural asymmetry on BIC resonance in these systems still requires further investigation.

This paper proposed an all-dielectric terahertz q-BIC metasurface based on a symmetry-broken rectangular pillar array. By introducing structural asymmetry, the q-BIC is induced by breaking the in-plane inversion (C_2) symmetry of the unit cell, achieving high *Q*-factors resonance. Compared with metallic THz BIC structures, the proposed design reduces ohmic losses and enhances local electromagnetic field confinement, thereby providing a more stable platform for virus detection. The study encompasses the following aspects: firstly, the generation mechanism of the BIC is explored through far-field scattering decomposition and near-field distribution analysis; secondly, the modulation of the BIC resonance by the degree of asymmetry is investigated, and the resonance *Q*-factors under varying asymmetric parameters are analyzed; thirdly, the sensing performance of the device for analytes with different refractive indices and thicknesses is evaluated; and finally, the q-BIC resonance is employed to detect two distinct bacteriophages, thereby validating the sensor's capability for theoretical virus differentiation.

2. Metasurface Design and Simulation

2.1. Metasurface Design

Figure 1a presents a schematic diagram of the designed metasurface. When illuminated by a normal incident *x*-polarized THz wave, the structure can excite the BIC mode. Figure 1b illustrates the detailed parameters of the metasurface unit cell: the length of the silicon pillar is L = 200 μm, with a height of h_1 = 200 μm. Symmetry breaking is introduced by removing rectangular blocks from the top-right and bottom-left corners. The removed block at the top-right corner has dimensions $w_1 \times w_2$ (for BIC, $w_1 = w_2$ = 50 μm), while that at the bottom-left corner is a square block of side length w_2 = 50 μm. The substrate has a thickness of h_2 = 300 μm, the period of the unit cell in both *x* and *y* directon are $P_x = P_y$ = 300 μm. By varying the length w_1 of the etched silicon pillar in the top-right corner, mirror symmetry along the *x*-direction can be broken to enable the excitation of the q-BIC mode.

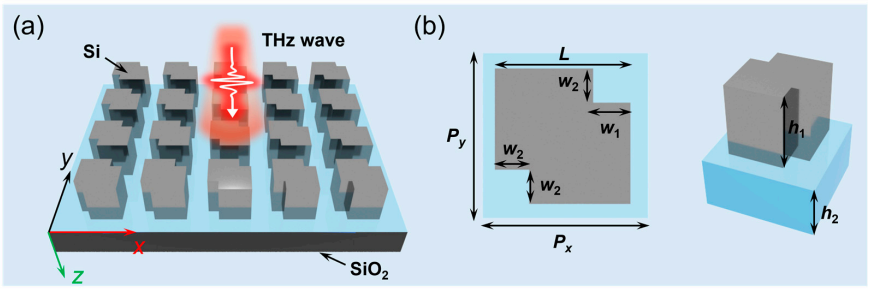


Figure 1. (**a**) Schematic of the designed metasurface, illuminated by normally incident *x*-polarized THz wave. (**b**) Top view of the unit cell with detailed parameters.

Most reported that symmetry-breaking q-BIC metasurfaces rely on multi-element unit cells—such as asymmetric dimers, tetramers, or pairs of pillars—where the perturbation is introduced by displacing, rotating, or resizing one element relative to another. In contrast, our design employs a single rectangular silicon pillar with two corner truncations, and the asymmetry is controlled solely by the truncation length w1 at one corner while the opposite corner is fixed. This is a fundamentally different perturbation mechanism: (a) it does not require multiple resonators or inter-element displacement; (b) it preserves a compact, single-element unit cell; and (c) it provides a single scalar parameter that directly and continuously tunes the radiative coupling of the q-BIC.

For simulation, the THz transmission characteristics of the designed metasurface were analyzed using Ansys Lumerical FDTD Solutions. In the simulations, a plane wave was incident along the *z*-direction, with the electric field polarized along the *x*-axis and the magnetic field along the *y*-axis. Periodic boundary conditions were applied in the *x* and *y* directions, while perfectly matched layers (PMLs) were adopted along the propagation direction to absorb outgoing radiation. The frequency sweep ranged from 0.64 to 0.66 THz, the refractive indices are taken as real values: Si (n = 3.4) and SiO_2 (n = 2.0) at the operating frequency, with loss tangents set to zero. More specific simulation settings can be found in the Supplementary Materials.

2.2. q-BIC Mode Induced by Symmetry Breaking

Figure 2a shows the transmission spectra of the metasurface for w_1 = 50 μm and w_1 = 40 μm, respectively. The black curve corresponds to the symmetric case (w_1 = 50 μm), where no resonance dip is observed in the spectrum. The red curve represents the transmission for w_1 = 40 μm. The asymmetry parameter is defined as $\delta = (w_2 - w_1)/w_2$, where w_1 is the truncation length at the top-right corner and w_2 = 50 μm is the fixed truncation length at the bottom-left corner. When $w_1 = w_2$ = 50 μm, δ = 0, corresponding to the fully symmetric structure that supports a symmetry-protected BIC. In our design, the removal of rectangular blocks from the top-right and bottom-left corners breaks the C_2 symmetry of the unit cell [48,49], which allows the previously bound mode to couple to free-space radiation. When an asymmetry of δ = 0.2 is introduced, an ultra-narrow resonance dip emerges around 0.648 THz. This observation indicates that the breaking of structural symmetry converts the BIC into a q-BIC, manifesting as a distinct spectral feature.

Since BIC and q-BIC resonances typically arise from the coupling or destructive interference of multiple radiation channels, multipole expansion has become a widely adopted approach for elucidating their underlying mechanisms. To further analyze the physical origin of the observed resonance, multipole expansion method was performed in the vicinity of the resonance frequency. This method decomposes the complex electromagnetic radiation into fundamental components, including electric dipole (ED), magnetic dipole (MD), toroidal dipole (TD), electric quadrupole (EQ), and magnetic quadrupole (MQ) [50,51].

The ED within the unit cell can be calculated by integrating the induced current J over the entire volume:

$$\mathrm{p} = \frac{i}{\omega}\int J dr, \tag{1}$$

with

$$J = -i\omega\varepsilon_0(n^2-1)E, \tag{2}$$

where ω denotes the angular frequency, E is the electric field, and ε_0 is the vacuum permittivity. Then the MD moments and TD moments of the unit cell can be expressed as

$$\begin{aligned} m &= \frac{1}{2c}\int (r\times J)dr, \\ T &= \frac{1}{10c}\int \left[(r\cdot J)r - 2r^2 J\right]dr, \end{aligned} \tag{3}$$

where c is the speed of light in vacuum. The EQ and MQ moments can be written as

$$\begin{aligned} Q^e_{\alpha\beta} &= \frac{1}{j2\omega}\int \left[r_\alpha J_\beta + r_\beta J_\alpha - \frac{2}{3}\delta_{\alpha\beta}(r\cdot J)\right]dr, \\ Q^m_{\alpha\beta} &= \frac{1}{3c}\int \left\{[r\times J]_\alpha r_\beta + [r\times J]_\beta r_\alpha\right\}dr, \end{aligned} \tag{4}$$

where δ is the Dirac delta function and the subscripts $\alpha, \beta = x, y, z$. The total scattering power is expressed in SI units as

$$P_{scat} = \frac{k^4\mu_0 c^3}{12\pi}\left| p + \frac{ik}{c}T\right|^2 + \frac{k^4\mu_0 c}{12\pi}|m|^2 + \frac{k^6\mu_0 c^3}{160\pi}|Q^e_{\alpha\beta}|^2 + \frac{k^6\mu_0 c}{160\pi}|Q^m_{\alpha\beta}|^2, \tag{5}$$

where k = ω/c is the wavenumber, and the permeability is set to μ_0 = 1 for simplicity. Figure 2b shows the normalized multipolar contributions at resonance, defined as the ratio of each multipolar scattering cross-section to the total scattering cross-section:

$$Normalized\ \text{contribution}_i = \frac{P_{sca,i}}{P_{sca,total}}. \tag{6}$$

At 0.648 THz, the scattering intensity of the MD far exceeds that of the EQ and MQ, while contributions from ED and TD are almost zero. This clearly indicates that MD radiation dominates at this frequency. Furthermore, in conjunction with the observations in Figure 2a, it can be inferred that once the mirror symmetry is broken, the originally symmetry-protected BIC mode weakly couples to the free-space continuum, enabling partial energy leakage into radiation channels and thereby giving rise to an extremely narrow q-BIC resonance in the transmission spectrum.

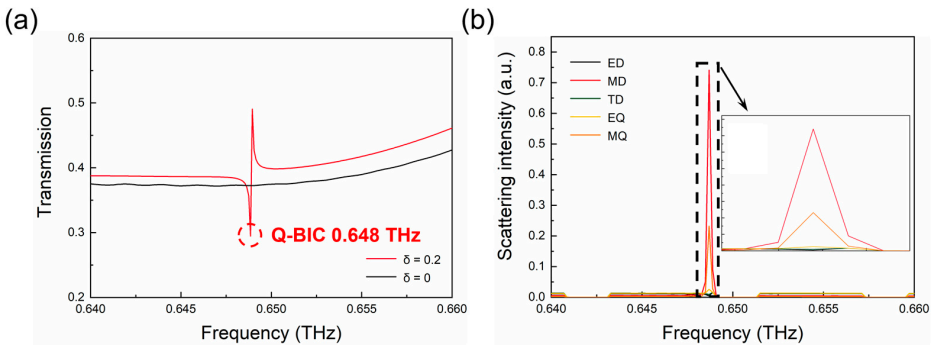


Figure 2. (**a**) The transmission spectra of symmetric structures (δ = 0) and asymmetric structures (δ = 0.2). (**b**) Multipole expansion analysis of the q-BIC mode.

To further analyze the formation mechanism of the resonance, we examined the electric field distribution inside the unit cell, as shown in Figure 3. The field distribution within symmetric unit cell at 0.648 THz was first analyzed; as shown in Figure 3a, the electric field is primarily concentrated at the edges of the silicon pillars, especially in the vicinity of the four truncated corners, whereas the field intensity in the central region remains relatively low. It should be emphasized that this weak driven field does not imply that the symmetry-protected BIC eigenmode lacks field confinement; rather, under normally incident plane wave excitation, the ideal symmetry-protected BIC cannot couple to the external radiation field. Therefore, the eigenmode is not excited, and the FDTD-driven field remains weak. In contrast, when mirror symmetry is broken (Figure 3b), the previously suppressed radiation channels become accessible, and the q-BIC mode can be efficiently excited. Under this condition, the electric field distribution changes markedly: the high-field regions are predominantly localized between the two truncated defects and form continuous enhanced areas along the diagonal direction. Compared with the symmetric case, the symmetry-broken structure exhibits significantly stronger field coupling, with the electromagnetic energy being effectively confined within the silicon architecture.

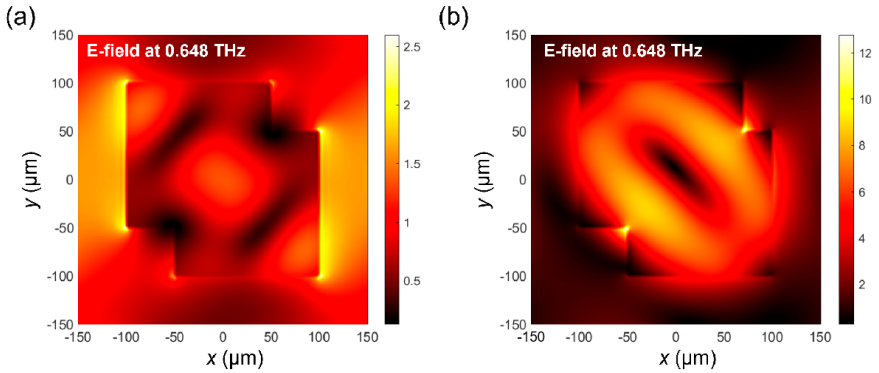


Figure 3. (**a**) The electric field distribution of the symmetric unit cell and the (**b**) symmetry-broken unit cell at 0.648 THz.

Quantitatively, the maximum electric field intensity is approximately 2.5 (in arbitrary units) for the symmetric structure, whereas after the mirror symmetry is broken and the q-BIC mode is formed, the peak local field increases to about 12, corresponding to an enhancement factor ($|E|/|E0|$) of roughly 4.8. This significant field enhancement originates from the intrinsically low radiation loss of the q-BIC mode, which allows electromagnetic energy to be confined within the resonant structure for a longer duration. In conjunction with the preceding multipole analysis, it can be concluded that the resonance is predominantly governed by the MD mode, and the enhanced MD response further facilitates the accumulation of electromagnetic energy inside the dielectric unit cell. Moreover, the strongly localized fields on and around the silicon resonator render the q-BIC resonance highly susceptible to perturbations in the refractive index of the surrounding medium. As a result, even minute changes in the ambient environment can induce measurable resonance frequency shifts, thereby substantially enhancing the sensor's sensitivity to trace analytes.

To investigate the influence of structural parameters on the tuning of BIC resonances, we systematically examined how variations in the truncation length w_1 affect the spectral response of the metasurface. The results are presented in Figure 4. Figure 4a displays the transmission characteristics as a function of both frequency and w_1. A clear transition from BIC to q-BIC is observed: as w_1 gradually decreases from 90 to 10 μm, the resonance frequency exhibits a monotonic redshift. Figure 4b compares the transmission spectra for different asymmetry parameters. When $\delta = 0$, no resonance dip is observed, indicating that the bound state is completely decoupled from the free-space continuum—a hallmark of

the symmetry-protected BIC. In contrast, when the unit cell possesses a finite asymmetry ($\delta \neq 0$), the transmission spectrum exhibits an asymmetric Fano line shape with a finite *Q*-factor. Specifically, while maintaining w_2 = 50 μm, as w_1 is decreased from its initial value of 50 μm to δ = 0.3, a sharp and narrow resonance dip emerges. When δ = 0.3, the resonance dip is sharper and narrower. Conversely, with w_1 fixed at 50 μm and w_2 gradually reduced, the same asymmetric parameter variation leads to a Fano-like transmission dip with extremely narrow linewidth, where the transmittance at resonance drops to nearly zero. As δ increases further, the resonance linewidth progressively broadens and the resonance frequency shifts, clearly demonstrating that by tuning the asymmetry parameter, the non-radiative BIC mode gradually evolves into a q-BIC mode with finite radiative characteristics.

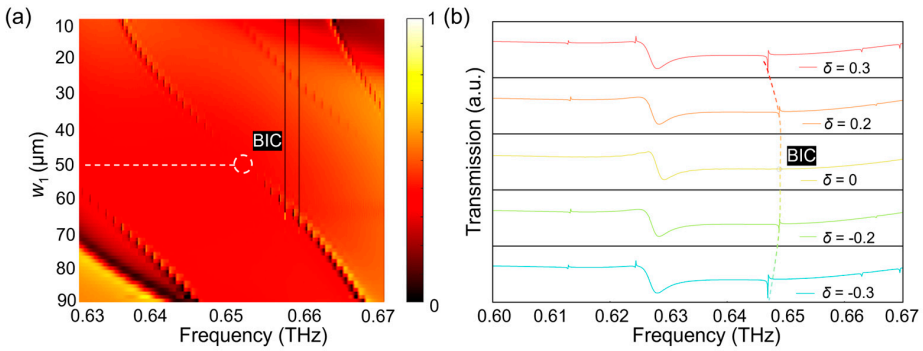


Figure 4. (**a**) The transmission characteristics as a function of both frequency and w_1. (**b**) The transmission spectrum when the asymmetric parameter δ = −0.3, −0.2, 0, 0.2, and 0.3.

To further examine the dependence of the *Q*-factor on the asymmetry parameter, Figure 5 presents the relationship between the *Q*-factor of the q-BIC and the asymmetry parameter δ. Figure 5a displays the transmission spectrum of the metasurface for δ = 0.3, where a distinct resonance dip is observed at 0.647 THz. The q-BIC resonance exhibits an asymmetric Fano line shape, which arises from the coupling between the discrete q-BIC mode and the continuum of free-space radiation. Therefore, Fano fitting is the natural and widely adopted approach for extracting the resonance frequency, linewidth, and *Q*-factor. Accordingly, the Fano model is adopted to fit the resonance curve for extracting the *Q*-factor, and the fitting expression is given as follows [52]:

$$\mathrm{T} = |a + ib + c/(\omega - \omega_0 + i\gamma)|, \tag{7}$$

where T represents the transmission coefficient, and ω_0 is the center frequency of the resonance peak; a, b, and c are fitting parameters, and γ is the damping rate. The *Q*-factor can be expressed as $Q = \omega_0/2\gamma$. Fitting of the simulation data yields a resonance *Q*-factor of 16,173 for the structure, with the fitted curve closely matching the simulated one (R^2 = 0.993). This confirms that symmetry breaking gives rise to a q-BIC mode featuring an ultra-high *Q*-factor. It is worth noting that the reported *Q*-factors are theoretical predictions under ideal conditions, and that experimental *Q* values will be limited by material absorption and fabrication tolerances. For example, Liu et al. experimentally measured Q ≈ 224 in a fabricated all-dielectric THz q-BIC biosensor [34].

For symmetry-protected q-BIC, the *Q*-factor and the asymmetry parameter δ are expected to follow the scaling relation $Q \propto 1/\delta^{-2}$. To verify this dependence, the *Q*-factors for various asymmetry parameters δ are calculated: Q > 80,000 at $\delta = \pm 0.1$, Q > 30,000 at $\delta = \pm 0.2$, as shown in Figure 5b. In the fully symmetric case (δ = 0), the theoretical *Q*-factor diverges to infinity, corresponding to an ideal BIC state. As the structural asymmetry progressively increases, regardless of the sign of δ, the *Q*-factor decreases rapidly

and exhibits a mirror-symmetric behavior about $\delta = 0$. The analysis confirms that the variation in the Q-factor with the asymmetry parameter indeed follows $Q \propto 1/\delta^{-2}$, which, in conjunction with our previous findings, further underscores the distinctive characteristics of resonances arising from the q-BIC mechanism. In addition, Figure S1 shows $1/Q$ versus δ^2 and provides a linear regression coefficient, which also confirms the expected inverse-square scaling in the limit of sufficiently small asymmetry.

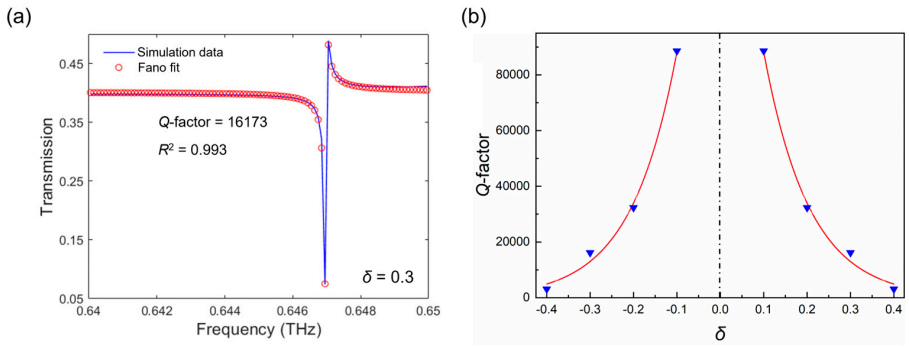


Figure 5. (**a**) Transmission spectrum of the metasurface and its Fano fitting curve when $\delta = 0.3$; (**b**) the relationship between the Q-factor and the symmetry-breaking parameter δ.

2.3. Refractive Index Sensing Performance of q-BIC

The q-BIC resonance frequency is sensitive to the surrounding refractive index, motivating a systematic exploration of the metasurface's sensing performance in the THz band. We first assessed the effect of analyte thickness, fixing the refractive index at $n = 1.1$ and varying the thickness from 5 to 25 μm in 5 μm steps. A blank measurement (without analyte) served as the control. As shown in Figure 6a, the resonance frequency exhibited a clear redshift upon analyte loading, with the redshift magnitude growing monotonically with increasing thickness. As the analyte thickness increased from 5 μm to 15 μm, the resonance frequency exhibited a pronounced redshift, indicating that the sensor is highly responsive to thickness variations. However, when the thickness was further increased to 20 μm and 25 μm, the resonance peak continued to redshift, albeit with a substantially reduced frequency shift.

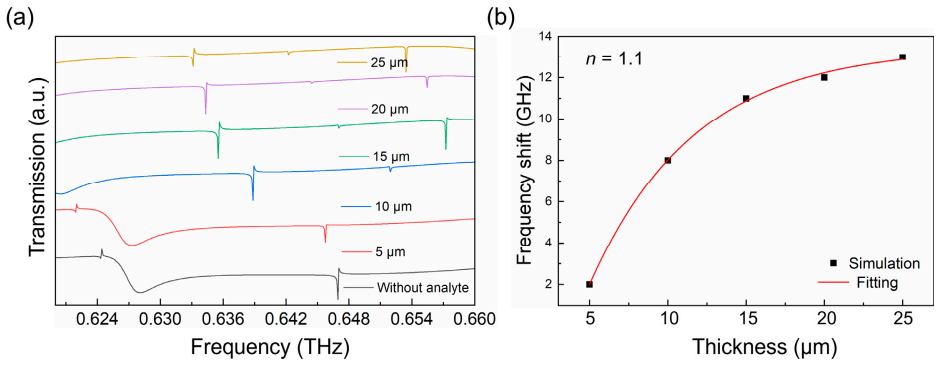


Figure 6. (**a**) Transmission spectra of the metasurface when fixing the refractive index at $n = 1.1$ with different analyte thickness. (**b**) The relationship between frequency shift and analyte thickness, along with the fitted curve.

To quantitatively characterize the relationship between analyte thickness and frequency shift, the measured resonance frequency shifts were fitted as a function of thickness. As shown in Figure 6b, the fitting results reveal that the frequency shift initially increases rapidly and then gradually saturates with increasing thickness. Notably, a significant

frequency shift is already achieved at an analyte thickness of approximately 15 μm. As the q-BIC resonance is strongly localized near the truncated corners of the silicon pillar, the electric field decays rapidly away from the metasurface. When the analyte thickness is smaller than the field decay length, essentially all of the analyte lies within the high-field region, so the frequency shift increases quickly with thickness. However, once the thickness exceeds the effective field decay length (about 15 μm in our design), the additional analyte is located in the weak-field region and contributes little to the resonance shift. Consequently, the sensitivity saturates beyond 15 μm. Therefore, this thickness was adopted for all subsequent refractive index sensing analyses.

With the analyte thickness fixed at 15 μm, we evaluated the sensor's response to varying refractive indices (Figure 7a). The resonance peak progressively redshifts as the refractive index increases, while the q-BIC mode retains a high Q-factor, confirming the structural robustness. The extracted frequency shifts show a nearly linear dependence on the refractive index (Figure 7b), indicating a consistent linear response over the tested range. Fitting the data yields a slope that defines the refractive index sensitivity (S) of the sensor:

$$S = \frac{\Delta f}{\Delta n}, \tag{8}$$

where Δf is the resonant frequency shift, Δn is the change in refractive index. The resonance frequency exhibits a redshift of about 11 GHz when the refractive index increases from 1.00 to 1.10 (Δn = 0.10 RIU), yielding a sensitivity of approximately 110 GHz/RIU for the proposed metasurface. This result confirms the excellent responsiveness of the q-BIC metasurface to refractive index changes.

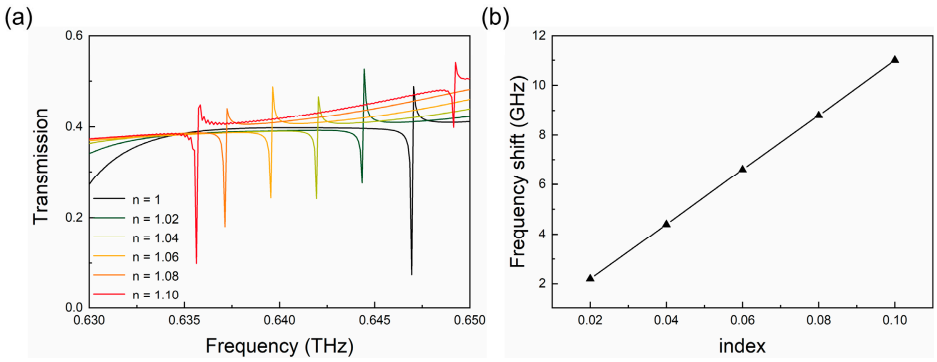


Figure 7. (**a**) Sensor's response to varying refractive indices. (**b**) The relationship between frequency shift and sample refractive index.

In addition, the Figure of Merit (FOM) is defined as FOM = S/FWHM, where S is the refractive index sensitivity and FWHM is the full width at half maximum of the resonance. For the q-BIC resonance at f = 0.647 THz with Q = 16,713, the FWHM is 0.05 GHz; thus, FOM = 2.19 × 10^3 RIU^{-1}. Then the minimum resolvable refractive index change can be defined as Δn_{min} = FWHM/S. For S = 110 GHz/RIU with FWHM = 0.05 GHz, the Δn_{min} = 4.56 × 10^{-5} RIU. The above results demonstrate that the designed metasurface exhibits excellent performance in refractive index sensing. This not only confirms its capability as a highly sensitive sensor but also reveals its considerable potential for biological detection.

3. Application Potential of q-BIC in Biosensing

Virus detection plays a critical role in disease prevention, public health safety, food safety, and environmental monitoring. Given that viruses are typically only tens to hundreds of nanometers in size and that early-stage infections involve extremely low analyte

concentrations, detection methods are required to be ultra-sensitive. Consequently, virus detection has become a topic of considerable interest in biosensing research. Compared with conventional chemical substances, viruses possess complex biological structures, making them ideal targets for evaluating sensor performance in practical biological contexts. Moreover, different viruses generally exhibit distinct refractive indices, which enables their discrimination based on resonance frequency shift measurements.

The high sensitivity of the designed metasurface to refractive index changes, as demonstrated above, suggests its promising potential for biosensing. To further verify this, we chose two typical bacteriophages—MS2 and PRD1—as the test analytes in simulations; their dielectric constants were found to be 3.92 and 3.57, respectively [53]. The virus analytes were modeled as homogeneous effective medium layers with a thickness of 15 μm, placed in the gaps of the unit cell, and no material loss was included in the main-text simulations. MS2 (single-stranded RNA) and PRD1 (double-stranded DNA) differ in nucleic acid type and thus exhibit distinct electromagnetic responses. Both are non-infectious to humans and have been widely used as model viruses in sensing studies, making them appropriate for comparative evaluation [54]. In our simulation, MS2 and PRD1 are model analytes with distinct effective refractive indices, used solely to evaluate the sensor's capability to resolve small dielectric differences, the impact of actual virus samples on test results has also been explained in the Supplementary Materials. In addition, this study assumes a dry, low-loss environment and does not account for material dispersion or absorption.

Figure 8 presents the simulation results, revealing a pronounced redshift of the q-BIC resonance. The MS2 virus, with its higher dielectric constant relative to PRD1, induces a notably larger redshift (>9 GHz). It is important to note that the proposed structure is a label-free refractive index transducer rather than a complete biosensor; without a biorecognition element, it cannot achieve target-specific detection. In fact, the presence of a functional layer will cause a baseline redshift of the q-BIC resonance, because it increases the effective refractive index in the vicinity of the metasurface. And the functional layer affects the sensitivity in two competing ways:

a. Positive effect: The layer can concentrate the target analyte near the hot spot, improving the overlap between the analyte and the high-field region. This can enhance the effective sensitivity compared with a bare metasurface.
b. Negative effect: The layer increases the distance between the analyte and the metasurface surface. If the layer is thicker than the field decay length, the analyte experiences a weaker field, reducing the sensitivity. In addition, the functional layer itself contributes to the total effective index change, which may partially saturate the resonance response.

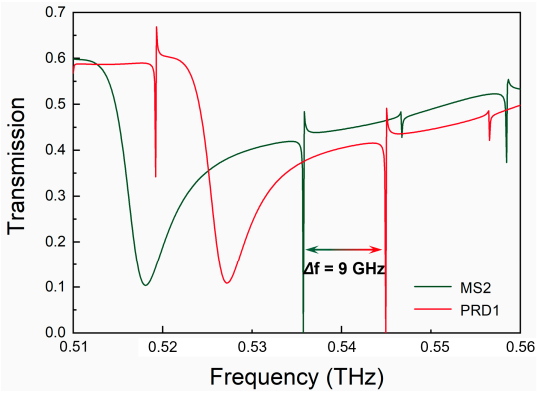


Figure 8. The transmission spectra for MS2 (green line) and PRD1 (red line).

For a thin functional layer, the negative effect is expected to be modest, and the net sensitivity may remain comparable to the bare metasurface. For thicker layers, the sensitivity would decrease. The functional layer may also introduce additional absorption or scattering losses, slightly broadening the resonance and reducing the *Q*-factor.

Furthermore, a comprehensive comparison between our proposed metasurface and other q-BIC metasurfaces in Table 1 evaluates key performance metrics including platform/material, operating spectral range, symmetry-breaking mechanism, dominant mode, numerical/experimental status, *Q*-factor, sensitivity/FOM, and biosensing target. Compared with these works, our design employs a single rectangular pillar with corner truncation as the symmetry-breaking mechanism. This provides a minimal, single-element geometry that is structurally simpler than multi-element dimers, tetramers, or nanohole arrays. The dominant mode is the magnetic dipole, which is distinct from the toroidal-dipole-dominated or electric-dipole-dominated q-BIC in many reported structures.

Table 1. Comparison with other q-BIC metasurfaces in recent work.

Year	Material	Spectral Range (THz)	Symmetry-Breaking Mechanism	Dominant Mode	Num./Exp.	*Q*-Factor	Sensitivity (GHz/RIU)	Biosensing Target	Reference
2026	AI + Polyimide	0.2–1.0	Asymmetry double split-ring	ED	Exp.	16	90	Glucose	[55]
2023	Cu + Polyimide	0.4–1.2	Asymmetric metallic hole arrays	\	Exp.	2044	147.7	PI film	[56]
2023	PEC + Polyethylene	0.3–0.6	Double-strip array	\	Num.	>500	87.5	\	[57]
2023	Si + SiO_2	0.76–0.84	Asymmetric silicon disks	mode I: MTD; mode III: ETD	Num.	mode I: 9×10^5; mode III: 5.1×10^6	mode I: 569.1 (liquid), 529 (gas); mode III: 532 (liquid), 498.3 (gas)	\	[58]
2021	Si + SiO_2	0.8–1.0	Asymmetric cylindrical holes	\	Num.	26,313	170.58	\	[59]
2023	Si/Quartz + Si	0.85–1.1	Asymmetric nano-elliptical cylinders	\	Num.	2219.1/1504.7	79.3/72.4	\	[60]
\	**Si + SiO_2**	**0.63–0.65**	**Corner truncation**	**MD**	**Num.**	**>80,000**	**110**	\	**This work**

4. Conclusions

In summary, we proposed a terahertz q-BIC biosensor based on a defect-engineered all-dielectric pillar metasurface, which achieves high-*Q* resonances and excellent sensing performance. This work encompasses four main aspects: (1) Symmetry breaking excites an MD-dominated q-BIC with a 4.8-fold local field enhancement. (2) The degree of structural asymmetry effectively modulates the q-BIC characteristics, enabling resonance excitation while maintaining a high *Q*-factor. (3) The effects of analyte refractive index and thickness on sensing performance are systematically investigated; the refractive index sensitivity reaches 110 GHz/RIU with an analyte thickness of only 15 μm. (4) The MS2 and PRD1 are employed as detection targets, and a resonance frequency difference of approximately 9 GHz is observed, enabling effective theoretical virus differentiation. The results in this work offer a promising platform for label-free THz biosensing.

Supplementary Materials: The following supporting information can be downloaded at: https://www.mdpi.com/article/10.3390/photonics13100920/s1, Figure S1. normalized multipolar contributions in the case of (a) δ = 0.3 and (b) δ = 0.3. (c) The evolution of normalized multipolar contributions versus δ. Figure S2. The magnetic field distribution of q-BIC at 0.648 THz. Figure S3. $1/Q$ versus δ^2 for the q-BIC resonance.

Author Contributions: Conceptualization, W.S. and X.W.; methodology, L.Z. and J.Z.; software, S.L. and X.D.; validation, W.S., X.Z. and W.N.; formal analysis, Z.R.; investigation, W.S. and S.L.; resources, W.S.; data curation, S.L.; writing—original draft preparation, S.L.; writing—review and editing, W.S.; visualization, L.Z.; supervision, X.W.; project administration, W.S.; funding acquisition, J.Z. All authors have read and agreed to the published version of the manuscript.

Funding: This research was funded by the National Natural Science Foundation of China, grant number 62605179, 62475121, 62435010, 62165006; the Natural Science Foundation of Jiangxi Province, grant number 20262BAC260001, 20252BEJ730361, 20242BAB20065, 20224ACB202004; the Jiangxi Province Ganpo Juncai Support Plan—High-Level and High-Skilled Leading Talent Training Project, grant number 2024–069; the Key Research and Development Program Project of Jiangxi Province, grant number 20243BBI91011; the Science and Technology Project Foundation of the Education Department of Jiangxi Province, grant number GJJ2401207; the Nanchang City Key Laboratory of Optic-electronic Detection and Information Processing, grant number 2019-NCZDSY−008; and the Doctoral Start-up Funding of Jiangxi Science & Technology Normal University, grant number 2024BSQD39, 2022BSQD02.

Institutional Review Board Statement: Not applicable.

Informed Consent Statement: Not applicable.

Data Availability Statement: No new data were created or analyzed in this study. Data sharing is not applicable to this article.

Conflicts of Interest: The authors declare no conflicts of interest.

References

1. Wang, Y.H.; Jia, K.Y.; Lin, J.H. Optical biosensors for the detection of foodborne pathogens: Recent development and future prospects. *TrAC Trends Anal. Chem.* **2024**, *177*, 117785. [CrossRef]
2. Zhang, Z.Y.; Wang, H.; Chen, Z.P.; Wang, X.; Choo, J.; Chen, L. Plasmonic colorimetric sensors based on etching and growth of noble metal nanoparticles: Strategies and applications. *Bissensors Bioelectron.* **2018**, *114*, 52–65. [CrossRef] [PubMed]
3. Hermannsson, P.G.; Sørensen, K.T.; Vannahme, C.; Smith, C.L.; Klein, J.J.; Russew, M.-M.; Grützner, G.; Kristensen, A. All-polymer photonic crystal slab sensor. *Opt. Express* **2015**, *23*, 16529–16539. [CrossRef] [PubMed]
4. Zhang, W.; Lin, J.; Yuan, Z.; Lin, Y.; Shang, W.; Chin, L.K.; Zhang, M. Terahertz Metamaterials for Biosensing Applications: A Review. *Biosensors* **2024**, *14*, 3. [CrossRef] [PubMed]
5. Panciera, C.; Brunetti, G.; Ciminelli, C. Numerical investigation of IgG sensing through nanoscale topological-assisted metasurface for liquid biopsy. *Nanotechnol. Rev.* **2026**, *15*, 20250284. [CrossRef]
6. Colapietro, P.; Brunetti, G.; Panciera, C.; Elicio, A.; Ciminelli, C. Shining the Path of Precision Diagnostic: Advancements in Photonic Sensors for Liquid Biopsy. *Biosensors* **2025**, *15*, 473. [CrossRef] [PubMed]
7. Chen, H.; Fan, X.; Fang, W.; Cao, S.; Sun, Q.; Wang, D.; Niu, H.; Li, C.; Wei, X.; Bai, C.; et al. Investigation of Multiple High Quality-Factor Fano Resonances in Asymmetric Nanopillar Arrays for Optical Sensing. *Photonics* **2024**, *11*, 68. [CrossRef]
8. Thara, R.L.; Priya, P.A. 1D topological photonic crystal based nanosensor for tuberculosis detection. *Nanotechnology* **2024**, *35*, 415204. [CrossRef] [PubMed]
9. di Toma, A.; Brunetti, G.; Colapietro, P.; Ciminelli, C. High-Resolved Near-Field Sensing by Means of Dielectric Grating with a Box-Like Resonance Shape. *IEEE Sens. J.* **2024**, *24*, 6045–6053. [CrossRef]
10. Dash, D.; Saini, J.; Goyal, A.K. Performance analysis of hyperbolic graded topological resonator for biosensing applications. *Sci. Rep.* **2025**, *15*, 9107. [CrossRef] [PubMed]
11. Wilmink, G.J.; Grundt, J.E. Invited Review Article: Current State of Research on Biological Effects of Terahertz Radiation. *J. Infrared Millim. Terahertz Waves* **2011**, *32*, 1074–1122. [CrossRef]
12. Yang, X.; Zhao, X.; Yang, K.; Liu, Y.; Liu, Y.; Fu, W.; Luo, Y. Biomedical applications of terahertz spectroscopy and imaging. *Trends Biotechnol.* **2016**, *34*, 810–824. [CrossRef] [PubMed]

13. Markelz, A.G. Terahertz dielectric sensitivity to biomolecular structure and function. *IEEE J. Sel. Top. Quantum Electron.* **2015**, *23*, 1–10.
14. Fischer, B.M.; Walther, M.; Jepsen, P.U. Far-infrared vibrational modes of DNA components studied by terahertz time-domain spectroscopy. *Phys. Med. Biol.* **2010**, *55*, 7875–7890.
15. Falconer, R.J.; Markelz, A.G. Terahertz spectroscopic analysis of peptides and proteins. *J. Infrared Millim. Terahertz Waves* **2012**, *33*, 973–988. [CrossRef]
16. Wang, H.; Zheng, F.; Xu, Y.; Mauk, M.G.; Qiu, X.; Tian, Z.; Zhang, L. Recent progress in terahertz biosensors based on artificial electromagnetic subwavelength structure. *TrAC Trends Anal. Chem.* **2023**, *158*, 116888. [CrossRef]
17. Zhao, S.; Fan, Y.; Yang, R.; Ye, Z.; Zhang, F.; Wang, C.; Luo, W.; Wen, Y.; Zhou, J. Smart reconfigurable metadevices made of shape memory alloy metamaterials. *Opto-Electron. Adv.* **2025**, *8*, 240109. [CrossRef]
18. Wang, C.; Tan, Y.; Wen, Y.; Zhao, S.; Yu, K.; Zhang, R.; Sun, J.; Zhou, J. Giant modulation of terahertz nonlinearity via photo-engineering intervalley transitions mediated by metasurfaces. *Mater. Today* **2026**, *97*, 103340. [CrossRef]
19. Shen, S.; Liu, X.; Shen, Y.; Qu, J.; Pickwell-MacPherson, E.; Wei, X.; Sun, Y. Recent advances in the development of materials for terahertz metamaterial sensing. *Adv. Opt. Mater.* **2022**, *10*, 2101008. [CrossRef]
20. Luk'Yanchuk, B.; Zheludev, N.I.; Maier, S.A.; Halas, N.J.; Nordlander, P.; Giessen, H.; Chong, C.T. The Fano resonance in plasmonic nanostructures and metamaterials. *Nat. Mater.* **2010**, *9*, 707–715. [CrossRef] [PubMed]
21. Zhang, S.; Genov, D.; Wang, Y.; Liu, M. Plasmon-induced transparency in metamaterials. *Phys. Rev. Lett.* **2008**, *101*, 047401. [CrossRef] [PubMed]
22. Fan, Y.; Zhang, F.; Shen, N.-H.; Fu, Q.; Wei, Z.; Li, H.; Soukoulis, C.M. Achieving a high-Q response in metamaterials by manipulating the toroidal excitations. *Phys. Rev. A* **2018**, *97*, 033816. [CrossRef]
23. Kuznetsov, A.I.; Miroshnichenko, A.E.; Brongersma, M.L.; Kivshar, Y.S.; Luk'yanchuk, B. Optically resonant dielectric nanostructures. *Science* **2016**, *354*, aag2472. [CrossRef] [PubMed]
24. Abujetas, D.R.; van Hoof, N.; ter Huurne, S.; Rivas, J.G.; Sánchez-Gil, J.A. From Fano resonances to bound states in the continuum in dipole arrays at THz frequencies. *Phys. Rev. B* **2019**, *99*, 155436.
25. Singh, R.; Cao, W.; Al-Naib, I.; Cong, L.; Withayachumnankul, W.; Zhang, W. Ultrasensitive terahertz sensing with high-*Q* Fano resonances in metasurfaces. *Appl. Phys. Lett.* **2014**, *105*, 171101. [CrossRef]
26. Zhang, J.; Mu, N.; Liu, L.; Xie, J.; Fenng, H.; yao, J.; Chen, T.; Zhu, W. Highly sensitive terahertz metamaterial biosensor with electromagnetically induced transparency for influenza virus identification. *Biosens. Bioelectron.* **2021**, *185*, 113241. [PubMed]
27. Yang, C.L.; Shen, Z.L.; Cui, Y.Q.; Zhang, N.; Zhang, L.; Yan, R.; Chen, X. Terahertz molecular vibrational sensing using 3D printed anapole meta-biosensor. *Biosens. Bioelectron.* **2025**, *278*, 117351. [CrossRef] [PubMed]
28. lotnik, Y.; Peleg, O.; Dreisow, F.; Heinrich, M.; Nolte, S.; Szameit, A.; Segev, M. Experimental observation of optical bound states in the continuum. *Phys. Rev. Lett.* **2011**, *107*, 183901. [CrossRef] [PubMed]
29. Hsu, C.; Zhen, B.; Lee, J.; Chua, S.-L.; Jonhson, S.G.; Joannopoulos, J.D.; Soljačić, M. Observation of trapped light within the radiation continuum. *Nature* **2013**, *499*, 188–191. [CrossRef] [PubMed]
30. Yoon, J.W.; Song, S.H.; Magnusson, R. Critical field enhancement of asymptotic optical bound states in the continuum. *Sci. Rep.* **2015**, *5*, 18301. [CrossRef] [PubMed]
31. Kupriianov, A.S.; Xu, Y.; Sayanskiy, A.; Dmitriev, V.; Kivshar, Y.S.; Tuz, V.R. Metasurface engineering through bound states in the continuum. *Phys. Rev. Appl.* **2019**, *12*, 014024. [CrossRef]
32. Ju, C.; Zhang, D.-Q.; Ma, Y.-B.; Wang, Y.; Fang, B.; Pan, G.-M.; Jin, Z.-W.; Hong, Z.; Chen, M.-M.; Lin, C.-Y.; et al. Thermally Tunable Quasi-Bound State in the Continuum and Electromagnetically Induced Transparency Analogue Based on the Hybrid Phase-Change Metasurfaces. *ACS Appl. Mater. Interfaces* **2026**, *18*, 36141–36150. [CrossRef] [PubMed]
33. Wang, C.; Liu, M.-S.; Zhang, D.-Q.; Jin, Z.-W.; Pan, G.-M.; Fang, B.; Hong, Z.; Shu, F.-Z. Active control of the toroidal dipole and quasi-bound state in the continuum based on the symmetric and asymmetric hybrid dumbbell aperture arrays. *Photonics Res.* **2025**, *13*, 1534–1543. [CrossRef]
34. Liu, M.S.; Zhou, H.P.; Zhang, D.Q.; Fang, B.; Pan, G.M.; Jin, Z.W.; Hong, Z.; Shu, F.Z. Dynamically tunable multiple quasi-bound states in the continuum based on the phase-change metasurface. *Photonics Res.* **2026**, *14*, 1348–1358. [CrossRef]
35. Liu, L.; Tian, J.; Zhao, G.; Wang, Z. A Q-BIC driven polarization-insensitive all-dielectric terahertz metasurface biosensor with a high experimental Q-factor. *Opt. Laser Technol.* **2025**, *192*, 114123. [CrossRef]
36. Panciera, C.; Brunetti, G.; Ciminelli, C.; Butt, M.A. Ultra-Broadband Metasurface Absorber Enabled by a Central-Bar-Coupled Split-Disk Dimer. *Biosensors* **2026**, *16*, 439. [CrossRef] [PubMed]
37. Hsu, C.W.; Zhen, B.; Stone, A.D.; Joannopoulos, J.D.; Soljačić, M. Bound states in the continuum. *Nat. Rev. Mater.* **2016**, *1*, 16048. [CrossRef]
38. Luo, M.; Zhou, Y.; Zhao, X.; Li, Y.; Guo, Z.; Yang, X.; Zhang, M.; Wang, Y.; Wu, X. Label-free bound-states-in-the-continuum biosensors. *Biosensors* **2022**, *12*, 1120. [CrossRef] [PubMed]

39. Kühner, L.; Sortino, L.; Berté, R.; Wang, J.; Ren, H.; Maier, S.A.; Kivshar, Y.; Tittl, A. Radial bound states in the continuum for polarization-invariant nanophotonics. *Nat. Commun.* **2022**, *13*, 4992. [CrossRef] [PubMed]
40. Schiattarella, C.; Sanità, G.; Alulema, B.G.; Lanzio, V.; Cabrini, S.; Lamberti, A.; Rendina, I.; Mocella, V.; Zito, G.; Romano, S.; et al. High-Q photonic aptasensor based on avoided crossing bound states in the continuum and trace detection of ochratoxin A. *Biosens. Bioelectron. X* **2022**, *12*, 100262. [CrossRef]
41. Huang, C.; Liang, L.; Chang, P.; Yao, H.; Yan, X.; Zhang, Y.; Xie, Y. Terahertz liquid biosensor based on a graphene metasurface for ultrasensitive detection with a quasi-bound state in the continuum. *Adv. Mater.* **2024**, *36*, e2310493. [CrossRef] [PubMed]
42. Wang, R.; Song, L.; Ruan, H.; Yang, Q.; Yang, X.; Zhang, X.; Jiang, R.; Shi, X.; Shkurinov, A.P. Ultrasensitive terahertz label-free metasensors enabled by quasi-bound states in the continuum. *Research* **2024**, *7*, 0483. [CrossRef] [PubMed]
43. Yang, Y.; Kravchenko, I.I.; Briggs, D.P.; Valentine, J. All-dielectric metasurface analogue of electromagnetically induced transparency. *Nat. Commun.* **2014**, *5*, 5753. [CrossRef] [PubMed]
44. Fang, C.; Yang, Q.; Yuan, Q.; Gan, X.; Zhao, J.; Shao, Y.; Liu, Y.; Han, G.; Hao, Y. High-Q resonances governed by the quasi-bound states in the continuum in all-dielectric metasurfaces. *Nanomaterials* **2022**, *12*, 2084. [PubMed]
45. Hsiao, H.H.; Hsu, Y.C.; Liu, A.Y.; Hsieh, J.C.; Lin, Y.H. Ultrasensitive refractive index sensing based on the quasi-bound states in the continuum of all-dielectric metasurfaces. *Adv. Opt. Mater.* **2022**, *10*, 2200812. [CrossRef]
46. Koshelev, K.; Bogdanov, A.; Kivshar, Y. Meta-optics and bound states in the continuum. *Sci. Bull.* **2020**, *65*, 1106–1124. [CrossRef] [PubMed]
47. Staude, I.; Miroshnichenko, A.E.; Decker, M.; Fofang, N.T.; Liu, S.; Gonzales, E.; Dominguez, J.; Luk, T.S.; Neshev, D.N.; Brener, I.; et al. Tailoring directional scattering through magnetic and electric resonances in subwavelength silicon nanodisks. *ACS Nano* **2017**, *4*, 585–591.
48. Koshelev, K.; Lepeshov, S.; Liu, M.; Bogdanov, A.; Kivshar, Y. Asymmetric Metasurfaces with High-Q Resonances Governed by Bound States in the Continuum. *Phys. Rev. Lett.* **2018**, *121*, 193903. [CrossRef] [PubMed]
49. Liu, Z.; Xu, Y.; Lin, Y.; Xiang, J.; Feng, T.; Cao, Q.; Li, J.; Lan, S.; Liu, J. High-Q Quasibound States in the Continuum for Nonlinear Metasurfaces. *Phys. Rev. Lett.* **2019**, *123*, 253901. [CrossRef] [PubMed]
50. Evlyukhin, A.B.; Reinhardt, C.; Seidel, A.; Luk'yanchuk, B.S.; Chichkov, B.N. Optical response features of Si-nanoparticle arrays. *Phys. Rev. B* **2014**, *90*, 205434.
51. Kaelberer, T.; Fedotov, V.A.; Papasimakis, N.; Tsai, D.P.; Zheludev, N.I. Toroidal dipolar response in a metamaterial. *Science* **2010**, *330*, 1510–1512. [CrossRef] [PubMed]
52. Feng, J.; Wang, X.; Shi, W.; Ma, L.; Ji, Y.; Fan, F.; Chang, S. Asymmetric dumbbell dimers simultaneously supporting quasi-bound states in continuum and anapole modes for terahertz biosensing. *Nanophotonics* **2024**, *13*, 4007–4017. [CrossRef] [PubMed]
53. Park, S.J.; Cha, S.H.; Shin, G.A.; Ahn, Y.H. Sensing viruses using terahertz nano-gap metamaterials. *Biomed. Opt. Express* **2017**, *8*, 3551–3558. [CrossRef] [PubMed]
54. Schijven, J.F.; Hassanizadeh, S.M. Removal of viruses by soil passage: Overview of modeling, processes, and parameters. *Crit. Rev. Environ. Sci. Technol.* **2000**, *30*, 49–127. [CrossRef]
55. Yan, Z.G.; Liu, P.H.; Zhou, H.P.; Liu, M.S.; Lin, C.Y.; Liu, T.T.; Zhang, D.Q.; Zhang, L.; Shu, F.Z. A dual-channel terahertz metasurface sensor based on polarization-dependent quasi-bound states in the continuum. *Opt. Lasers Eng.* **2026**, *202*, 109744. [CrossRef]
56. Liu, D.; Yu, X.; Wu, F.; Du, W.; Chen, L.; Liu, F.; Kuwahara, M.; Ono, S. Terahertz asymmetric metallic hole arrays with polarization-independent quasi-bound states in the continuum for membrane sensing. *Opt. Express* **2023**, *31*, 23608–23620. [CrossRef] [PubMed]
57. Shen, Y.; Wang, J.; Sheng, H.; Li, X.; Yang, J.; Liu, H.; Liu, D. Double-strip array-based metasurfaces with bICs for terahertz thin membrane detection. *Micromachines* **2024**, *15*, 43. [CrossRef] [PubMed]
58. Saadatmand, S.B.; Ahmadi, V.; Hamidi, S.M. Quasi-BIC based all-dielectric metasurfaces for ultra-sensitive refractive index and temperature sensing. *Sci. Rep.* **2023**, *13*, 20625. [CrossRef] [PubMed]
59. Li, Z.; Xiang, Y.; Xu, S.; Dai, X. Ultrasensitive terahertz sensing in all-dielectric asymmetric metasurfaces based on quasi-BIC. *J. Opt. Soc. Am. B* **2021**, *39*, 286–291. [CrossRef]
60. Yang, N.; Lang, T.; Cen, W.; Yu, Z.; Xiao, M.; Zhang, J.; Qiu, Y. Performance comparison of two terahertz all-dielectric metasurfaces based on bound states in the continuum. *J. Opt. Soc. Am. B* **2023**, *40*, 366–372. [CrossRef]

Disclaimer/Publisher's Note: The statements, opinions and data contained in all publications are solely those of the individual author(s) and contributor(s) and not of MDPI and/or the editor(s). MDPI and/or the editor(s) disclaim responsibility for any injury to people or property resulting from any ideas, methods, instructions or products referred to in the content.